JACS
JOURNAL OF THE AMERICAN CHEMICAL SOCIETY
pubs.acs.org/JACS
Article

Pt–Co@Pt Octahedral Nanocrystals: Enhancing Their Activity and Durability toward Oxygen Reduction with an Intermetallic Core and an Ultrathin Shell

Minghao Xie, Zhiheng Lyu, Ruhui Chen, Min Shen, Zhenming Cao, and Younan Xia*

Cite This: J. Am. Chem. Soc. 2021, 143, 8509–8518
Read Online
ACCESS | Metrics & More | Article Recommendations | Supporting Information

ABSTRACT: Despite extensive efforts devoted to the synthesis of Pt–Co bimetallic nanocrystals for fuel cell and related applications, it remains a challenge to simultaneously control atomic arrangements in the bulk and on the surface. Here we report a synthesis of Pt–Co@Pt octahedral nanocrystals that feature an intermetallic, face-centered tetragonal Pt–Co core and an ultrathin Pt shell, together with the dominance of {111} facets on the surface. When evaluated as a catalyst toward the oxygen reduction reaction (ORR), the nanocrystals delivered a mass activity of 2.82 A mg^{-1} and a specific activity of 9.16 mA cm^{-2}, which were enhanced by 13.4 and 29.5 times, respectively, relative to the values of a commercial Pt/C catalyst. More significantly, the mass activity of the nanocrystals only dropped 21% after undergoing 30 000 cycles of accelerated durability test, promising an outstanding catalyst with optimal performance for ORR and related reactions.

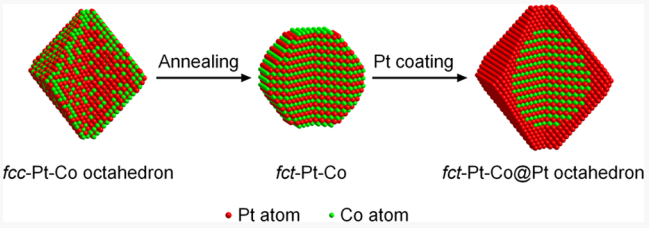

INTRODUCTION

Platinum-based nanocrystals are the most viable catalysts toward oxygen reduction, a cathode reaction key to the operation of multiple energy conversion devices such as fuel cells and metal–air batteries.[1−5] Due to the limited supply and increased cost of Pt, there is an urgent need to reduce the amount of Pt in a catalyst without compromising its performance. To this end, different strategies have been explored, including (i) alloying a less expensive transition metal M such as Fe, Co, Ni, and Cu with Pt to alter the electronic structure of Pt through the ligand effect;[6−12] (ii) constructing a core–shell structure by depositing Pt atoms on the surface only to improve their utilization efficiency while inducing the strain effect;[13−19] and (iii) engineering the shape of the catalytic particles to control the arrangement of surface atoms and thus leverage the facet effect.[15,16,19−22] All these strategies can be used to enhance the specific activity by weakening the binding energy of oxygen species (E_0) relative to that of the conventional Pt catalyst.[18,23−25] Specifically, a rich variety of bi- and even trimetallic nanocrystals with controlled compositions, lattice strains, and surface structures have been developed to achieve greatly enhanced activities toward the oxygen reduction reaction (ORR).

Theoretical calculations have predicted that alloying Pt with Co could result in an optimal E_0 and thus highly active ORR catalysts for use in acidic media, and the results have been confirmed by a number of experimental studies.[24,26−28] Typically, the Pt–Co alloys adopt a face-centered cubic (*fcc*) structure in the form of disordered solid solutions, in which the Pt and Co atoms are randomly distributed and the active sites tend to be structurally different. Under the highly corrosive ORR condition, dealloying will start on the surface and subsequently move into the interior, resulting in compromised performance due to the extensive Co loss and a defective Pt surface with low-coordination atoms. Since the discovery of Pt–Co intermetallic compounds with atomically ordered structures, tuning the crystal phase of Pt–Co nanocrystals has provided an additional strategy for pushing their catalytic performance to new levels.[26,28−31] Especially, at a Pt:Co molar ratio of 1:1, the intermetallic compound adopts a face-centered tetragonal (*fct*) structure (also known as an $L1_0$ structure) to enable a strong coupling between the Co(3d) and Pt(5d) atomic orbitals along the crystallographic *c* direction, stabilizing Co atoms against electrochemical oxidation and leaching.

To improve the utilization efficiency of Pt atoms, core–shell structures have been developed by depositing Pt as ultrathin overlayers on a less-expensive substrate.[16,19] However, conventional core–shell structures involving an *fcc* phase for the entire particle are prone to surface migration and core–shell interdiffusion, contributing to the dissolution of atoms from the core under the electrochemical conditions and thus degrading the ORR activity.[32] This issue can be mitigated by

Received: April 20, 2021
Published: May 27, 2021

https://doi.org/10.1021/jacs.1c04160
J. Am. Chem. Soc. 2021, 143, 8509–8518

switching to an intermetallic Pt−Co core because the mobilities of both Pt and Co atoms will be greatly reduced due to the increased lattice mismatch between the core and the shell. As nicely demonstrated by Sun and co-workers, $L1_0$-PtCo nanoparticles featuring a pseudospherical shape and a Pt-terminated surface exhibited great enhancement in terms of compositional stability and ORR durability.[28] In addition, different from the commonly explored Pt surface with an equi-biaxial strain, the $L1_0$ structure is expected to generate anisotropic surface strains different in magnitude along various directions.[33] Most recently, Sun and co-workers developed an eigenforce model to systematically investigate such anisotropic strains, demonstrating that the anisotropically strained Pt{111} surface was favorable for the dissociative mechanism of ORR.[33] Moreover, it is well known that the specific activity on the low-index, single-crystal Pt surfaces decreased in the order Pt{110} ≈ Pt{111} ≫ Pt{100} in aqueous $HClO_4$ solution.[7,18−20,22] Although the facets on intermetallic Pt−Co catalysts play an important role in determining their activity, it has been difficult to combine the benefits from faceting and atomic ordering because the disordered-to-ordered phase transition is typically achieved at a temperature above 500 °C. At such a high temperature, surface reconstruction will occur, transforming the nanocrystals enclosed by a set of specific facets to pseudospherical particles featuring a mix of different facets on the surface. To our knowledge, prior studies of Pt−Co intermetallic compounds have mainly attempted to reduce the particle size, tune the composition, and/or improve the atomic ordering, with essentially no report on how to control the facets exposed on the surface for further augmentation of ORR activity.[26,28−31,34−38]

Herein, we demonstrate a facile synthesis of bimetallic octahedral nanocrystals consisting of an *fct*-Pt−Co intermetallic core and three or four atomic layers of Pt shell terminated in {111} facets, together with a uniform size of 8 nm. Different from the reported $L1_0$-PtCo nanoparticles that lacked control over the surface structure,[28,29] the current system presents a well-defined Pt{111} surface to further augment the ORR activity. The fabrication of *fct*-Pt−Co@Pt nanocrystals with an octahedral shape critically relies on our ability to control the kinetics for the deposition and diffusion of Pt atoms on the surface of *fct*-Pt−Co seeds. Since no colloidal stabilizer or capping agent is involved in the Pt deposition process, the resultant nanocrystals feature a surfactant-free surface and can be directly used for electrochemical measurements without any cleaning.[39,40] Significantly, the successful creation of intermetallic octahedral nanocrystals with well-controlled crystal and surface structures offers an opportunity to examine the effects of both interior phase and exterior facets on ORR activity. When benchmarked against *fcc*-Pt−Co octahedral nanocrystals, *fct*-Pt−Co truncated octahedral nanocrystals, and a commercial Pt/C catalyst, the *fct*-Pt−Co@Pt octahedral nanocrystals exhibit over 5-, 3-, and 13-fold enhancement, respectively, in mass activity toward ORR. Markedly, the *fct*-Pt−Co@Pt nanocrystals deliver the highest specific and mass activities among all the Pt−Co bimetallic catalysts reported in the literature, and the mass activity only drops 21% after 30 000 cycles of accelerated durability test.

EXPERIMENTAL SECTION

Chemicals and Materials. All the chemical reagents were used as received from Sigma-Aldrich unless specified. These include platinum(II) acetylacetonate ($Pt(acac)_2$, 97%), cobalt(II) acetylacetonate ($Co(acac)_2$, ≥99.0%), tungsten hexacarbonyl ($W(CO)_6$, 99.99%), oleylamine (OAm, 70%), benzyl alcohol (BA, ≥99.5%), potassium tetrachloroplatinate(II) (K_2PtCl_4, 99.99%), citric acid (CA, 99.5%), and carbon black (Vulcan XC-72, Cabot). All aqueous solutions were prepared using deionized (DI) water with a resistivity of 18.2 MΩ cm at room temperature.

Synthesis of Pt−Co Octahedral Nanocrystals. In a standard synthesis, $Pt(acac)_2$ (0.025 mmol), $Co(acac)_2$, (0.039 mmol), $W(CO)_6$ (0.142 mmol), and OAm (3 mL) were mixed in BA (7 mL) and heated to 60 °C for 20 min under magnetic stirring and argon protection. The temperature was then increased to 200 °C at a ramping rate of 10 °C min^{-1} and kept at 200 °C for 40 min before the mixture was naturally cooled to room temperature. The solid products were collected by adding ethanol (15 mL) and acetone (5 mL) and then centrifuged at 6000 rpm for 10 min. The nanocrystals were dispersed in hexane (0.45 mg mL^{-1} Pt) for further use.

Preparation of Carbon-Supported Pt−Co Octahedral Nanocrystals (*fcc*-Pt−Co/C). In a typical process, 5 mL of the suspension of Pt−Co octahedral nanocrystals was mixed with 20 mg of carbon black in 20 mL of hexane under ultrasonication for 10 min to achieve a Pt loading of ca. 10 wt %. The mixture was then ultrasonicated for 3 h. The resultant *fcc*-Pt−Co/C was collected by centrifugation at 12 000 rpm for 15 min and dried in an oven set to 70 °C for 1 h.

Preparation of Carbon-Supported Pt−Co Intermetallic Nanocrystals (*fct*-Pt−Co/C). The carbon-supported Pt−Co octahedral nanocrystals were annealed under 96% Ar and 4% H_2 at 600 °C for 4 h to convert the Pt−Co alloy into an ordered, intermetallic compound. The actual loading of *fct*-Pt−Co nanocrystals on carbon was then determined using inductively coupled plasma mass spectrometry (ICP-MS). The resulting *fct*-Pt−Co/C was redispersed in DI water (0.2 mg mL^{-1} Pt) for further use.

Synthesis of Carbon-Supported Intermetallic Octahedral Nanocrystals Covered by an Ultrathin Skin of Pt (*fct*-Pt−Co@Pt/C). Typically, 5 mL of a suspension of the *fct*-Pt−Co nanocrystals on a carbon support and citric acid (30 mg) were mixed in a 20 mL vial. The mixture was ultrasonicated for 5 min, followed by heating at 80 °C for 10 min under magnetic stirring. When the temperature was stabilized, 1.5 mL of an aqueous solution containing K_2PtCl_4 (3.0 mg mL^{-1}) was added dropwise with a syringe pump at a rate of 0.1 mL h^{-1}. After completion, the reaction solution was kept at 80 °C for 9 h under magnetic stirring and then cooled to room temperature. The solid products were collected by centrifugation at 10 000 rpm for 10 min and dried in an oven set to 70 °C for 30 min prior to ORR measurement.

Characterizations. Transmission electron microscopy (TEM) images were taken using an HT-7700 microscope (Hitachi). High-angle annular dark-field and bright-field scanning transmission electron microscopy (HAADF- and HAABF-STEM, respectively) images and energy-dispersive X-ray (EDX) spectroscopy mapping data were acquired on an aberration-corrected Hitachi HD-2700 STEM. ICP-MS (NexION 300Q, Perkin−Elmer) was used to determine the metal contents in the as-obtained catalysts. X-ray diffraction (XRD) patterns were obtained with a PANalytical X'Pert PRO Alpha-1 diffractometer using a 1.8 kW ceramic copper tube source. The X-ray photoelectron spectroscopy (XPS) data were collected on a Thermo K-Alpha spectrometer with an Al Kα source.

Electrochemical Measurements. Approximately 2.0 mg of the *fct*-Pt−Co@Pt/C catalyst was dispersed in a solvent containing 1 mL of water, 1 mL of isopropanol alcohol, and 8 μL of 5 wt % Nafion (Aldrich) under sonication for 40 min. The concentration of Pt in the dispersion was quantified by ICP-MS. The as-obtained suspension was deposited on a precleaned glassy carbon rotating disk electrode (Pine Instruments) with a Pt loading of 1 μg and dried under ambient conditions. For the commercial Pt/C catalyst (20 wt % 3.2 nm Pt particles deposited on Vulcan XC-72, Premetek Co.), the Pt loading was 2 μg. A Pt coil and a HydroFlex reference electrode (Gaskatel) were used as the counter and reference electrodes, respectively. A home-built reversible hydrogen electrode (RHE) was used to calibrate the potentials of the reference electrode before using.

https://doi.org/10.1021/jacs.1c04160
J. Am. Chem. Soc. 2021, 143, 8509−8518

After loading of catalyst, the electrode was cycled in a N_2-saturated 0.1 M $HClO_4$ solution at a scanning rate of 50 mV s^{-1} in the potential range of 0.05−1.1 V_{RHE} until stable cyclic voltammograms (CVs) were collected. The electrochemical active surface area (ECSA) of the catalyst was derived from the average charges associated with the adsorption and desorption of hydrogen between 0.05 and 0.4 V_{RHE}, taking a value of 210 μC cm^{-2} for monolayer adsorption of hydrogen on the Pt surface. The ORR polarization curves were measured in the potential range of 0.05−1.1 V_{RHE} in an O_2-saturated 0.1 M $HClO_4$ solution at room temperature at a scanning rate of 20 mV s^{-1} and a rotation speed of 1600 rpm. All the electrochemical measurements were performed on a CHI600E potentiostat (CH Instruments). For the accelerated durability test (ADT), the CV and ORR polarization curves were measured after sweeping 10 000, 20 000, and 30 000 cycles in the range of 0.6−1.1 V_{RHE} at a rate of 100 mV s^{-1}, together with a rotation speed of 1600 rpm, in an O_2-saturated 0.1 M $HClO_4$ solution at room temperature.

RESULTS AND DISCUSSION

Synthesis and Characterization of *fct*-Pt−Co@Pt Octahedral Nanocrystals. Figure 1 shows the major steps

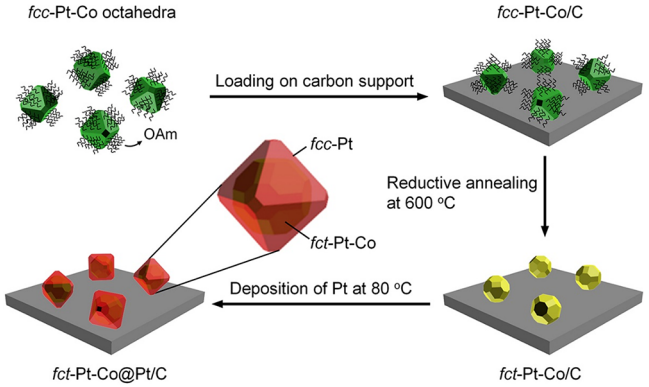

Figure 1. Schematic illustration of the three major steps involved in a typical synthesis of *fct*-Pt−Co@Pt/C catalyst. The Pt−Co octahedral nanocrystals with a disordered, *fcc* structure are loaded on a carbon support, followed by reductive annealing under H_2 and Ar to form an intermetallic phase featuring an ordered, *fct* structure. The surface of each Pt−Co intermetallic nanocrystal is then coated with a conformal, ultrathin shell made of Pt for the generation of an *fct*-Pt−Co@Pt octahedral nanocrystal.

involved in a synthesis of carbon-supported *fct*-Pt−Co@Pt nanocrystals. In the first step, *fcc*-Pt−Co octahedral nanocrystals enclosed by {111} facets, together with an average size of 6.3 ± 1.0 nm, were prepared using an oil-phase method (Figure S1). Typically, the $Pt(acac)_2$, $Co(acac)_2$, and $W(CO)_6$ were mixed with OAm in BA and then heated at 60 °C under Ar protection, followed by heating at 200 °C for 40 min. The presence of $W(CO)_6$ was key to the formation of *fcc*-Pt−Co nanocrystals with an octahedral shape. At the reaction temperature, $W(CO)_6$ was supposed to decompose into W atoms and CO molecules, which then served as a reducing agent for the initial reduction of Pt(II) ions and a capping agent for the {111} facets, respectively.[9,10] The nanocrystals were then loaded on carbon black (Figure S2A, denoted *fcc*-Pt−Co/C) and thermally annealed in a reductive atmosphere. The loading of Pt was kept at a relatively low level of about 10 wt % (confirmed by ICP-MS) to alleviate agglomeration when subjected to thermal treatment. During annealing, the nanocrystals experienced a slight size increase (7.1 ± 1.8 nm) and minor shape deformation to evolve into truncated octahedra. The final product is denoted *fct*-Pt−Co/C (Figure S2B). The sample was then conformally coated with an ultrathin shell of Pt to generate *fct*-Pt−Co@Pt octahedral nanocrystals with an average size of 8.4 ± 1.5 nm. The detailed structural and surface changes of the Pt−Co nanocrystals during the synthesis are illustrated in Figure S3A and B, respectively.

Figure 2A shows a TEM image of the final product prepared using the standard protocol, demonstrating the formation of

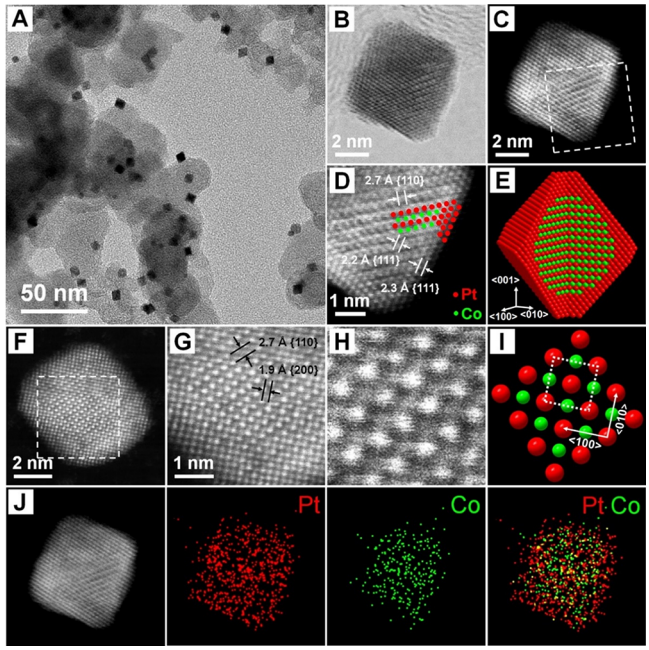

Figure 2. Characterizations of the *fct*-Pt−Co@Pt octahedral nanocrystals supported on carbon. (A) TEM image. (B) HAABF- and (C) HAADF-STEM images of a nanocrystal along the [1−10] direction. (D) Atomic-resolution STEM image taken from the corner region marked by a box in panel (C). (E) Schematic of the nanocrystal featuring an intermetallic core, a Pt shell of about three atomic layers thick, and {111} facets. The red- and green-colored atoms correspond to Pt and Co, respectively. (F) HAADF-STEM images of a nanocrystal along the [001] direction. (G, H) Atomic-resolution STEM image taken from the region marked by a box in panel (F). (I) 2D atomic model of the *fct*-Pt−Co structure along the [001] direction. (J) HAADF-STEM image and EDX mapping (Pt/red, Co/green) of a nanocrystal, revealing the spatial distributions of Pt and Co atoms.

octahedral nanocrystals with a uniform size and well-defined {111} facets, together with a good dispersion on the carbon support. Figure 2, B and C, shows HAABF- and HAADF-STEM images, respectively, of an individual nanocrystal projected along the [1−10] zone axis. The atomic-resolution STEM images suggest that the nanocrystal was composed of a highly ordered intermetallic core with alternating Pt and Co atomic layers, as well as a smooth Pt shell of three or four atomic layers in thickness (Figure 2D). The fast Fourier transform (FFT) pattern derived from the atomic image further confirms the tetragonal crystal structure (Figure S4, A and B). The lattice fringe spacing of 2.2 and 2.7 Å in the core could be assigned to the {111} and {110} planes of *fct*-Pt−Co, respectively. Remarkably, we observed a lattice fringe spacing of 2.3 Å for the {111} planes of the Pt shell, indicating the formation of an *fcc*-Pt shell on the Pt−Co core with an *fct*

https://doi.org/10.1021/jacs.1c04160
J. Am. Chem. Soc. 2021, 143, 8509−8518

structure. The 3D model of the nanocrystal is shown in Figure 2E. When the nanocrystal was projected along the [001] direction, a layer-by-layer atomic arrangement is clearly identified by the large difference in *Z*-contrast between Pt and Co atoms, together with a lattice fringe spacing of 1.9 Å for the {200} planes of *fct*-Pt−Co (Figure 2, F and G). As shown in Figure 2, H and I, the unit cell consists of a periodic square array of Co columns surrounded by Pt columns at the corners of each unit cell. The corresponding FFT result also confirms the *fct* structure along the [001] direction, which is consistent with a previous report (Figure S5).[41] The spatial distributions of Pt and Co were resolved by EDX mapping (Figure 2J). According to the mapping data, the Co atoms were mainly distributed in the core, while the Pt atoms were evenly distributed across the entire nanocrystal, confirming the formation of a core−shell structure. The elemental composition of the nanocrystals was also analyzed by ICP-MS to give a Pt/Co atomic ratio of 1.17 (Table S1).

We confirmed the phase transition of the Pt−Co nanocrystals by XRD. As shown in Figure 3, the as-synthesized Pt−Co

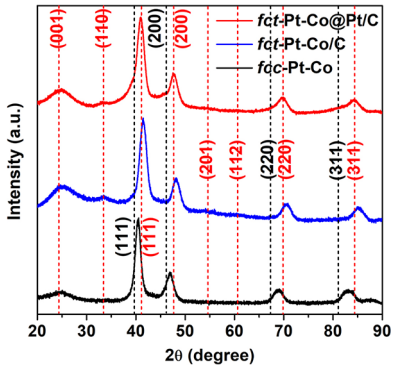

Figure 3. XRD patterns recorded from the samples of *fcc*-Pt−Co, *fct*-Pt−Co/C, and *fct*-Pt−Co@Pt/C, respectively. Black dashed lines: JCPDS #04-0802 (Pt). Red dashed lines: JCPDS #65-8969 (*fct*-PtCo).

nanocrystals exhibited an *fcc* structure typical of Pt (JCPDS #04-0802) with a slight shift to higher 2θ values for the diffraction peaks, indicating the replacement of some Pt atoms (radius: 1.39 Å) with smaller Co atoms (radius: 1.26 Å) and thus the reduction in lattice constant (Table S2). After reductive annealing at 600 °C for 4 h, an ordered *fct* diffraction pattern appeared and the diffraction peaks at about 24° and 33° can be assigned to *fct*-(001) and *fct*-(110) superlattice peaks of *fct*-Pt−Co (JCPDS# 65-8969), respectively. In addition, the (111) diffraction peak was shifted to a larger value, which can be attributed to a further alloying between Pt and Co and thus an additional lattice contraction of 1.6% along the [100] and [010] directions and 3.9% along the [001] direction, respectively, relative to the disordered *fcc* lattice (Table S2). After conformal deposition of Pt, all the characteristic peaks were well preserved in terms of position and full width at half-maximum, suggesting that the overgrowth of Pt skin did not cause any change to the *fct* structure and the domain size. The minor down-shift of the (111) diffraction peak suggests a slight increase of Pt content in the nanocrystals. Interestingly, the diffraction peaks of the *fct*-Pt−Co@Pt nanocrystals displayed an asymmetric shape because of the lattice mismatch between *fct*-Pt−Co and *fcc*-Pt.[42] There should be a relatively large lattice strain at the *fct*−*fcc* interface.

Mechanistic Understanding of the Synthesis. We used XPS to elucidate possible changes to the electronic structure of the nanocrystals during the annealing process. Figure S6 shows the XPS spectra collected from the Pt−Co nanocrystals before and after the thermal treatment. For the *fcc*-Pt−Co nanocrystals, the binding energy of the Pt 4f peak was positively shifted by 0.13 eV relative to that of pure Pt, indicating the alloying between Pt and Co and thus modification to the electronic structure of Pt (Figure S6A).[10] After reductive annealing, the binding energy of Pt $4f_{5/2}$ and $4f_{7/2}$ increased from 74.41 and 71.13 eV for the *fcc*-Pt−Co nanocrystals to 74.93 and 71.60 eV for the *fct*-Pt−Co nanocrystals, respectively, revealing an upshift of about 0.5 eV. The increase in binding energy could be attributed to the further diffusion of Co atoms into the Pt lattice and changes to the distribution of electrons. From the Co 2p spectra of the pristine sample, both metallic Co (Co $2p_{1/2}$ at 793.45 eV and Co $2p_{3/2}$ at 778.32 eV) and Co(II) (Co $2p_{1/2}$ at 797.10 eV and Co $2p_{3/2}$ at 781.22 eV) could be identified in the *fcc*-Pt−Co nanocrystals, corresponding to the Co atoms in the alloy phase and the cobalt oxide layers on the surface (Figure S6B).[29] The cobalt oxide layers have been suggested as a critical component for the generation of a highly ordered *fct*-Pt−Co structure during phase transition.[29,36] The reductive annealing could easily remove the oxygen on the surface, introducing defects and vacancies to lower the interdiffusion barrier between Pt and Co and thus increasing the atomic mobility for phase transition. As a result, the signals from metallic Co were greatly increased for the annealed sample. Meanwhile, as a substantial additive and reducing agent, the $W(CO)_6$ can introduce a third metallic component into the product. Therefore, the W 4f spectra were also collected to confirm the content and valence state of W in the samples before and after annealing (Figure S6C). The results revealed that the W existed as W(VI) or WO_3 (W $4f_{5/2}$ at 37.56 eV and W $4f_{7/2}$ at 35.44 eV) in the *fcc*-Pt−Co nanocrystals, suggesting the integration of W into the surface cobalt oxide layers. After annealing, additional W $4f_{5/2}$ and $4f_{7/2}$ peaks corresponding to W(IV) or WO_2 emerged in the *fct*-Pt−Co nanocrystals, suggesting the reduction of WO_3 during the reductive annealing (Figure S4C). Based on the results from XPS and XRD studies, Figure S7 provides a summary of major changes to the nanocrystals during the reductive annealing process.

Figure 4 shows the XPS spectra of the *fct*-Pt−Co@Pt octahedral nanocrystals. After conformal deposition of Pt, the binding energy of Pt $4f_{5/2}$ and $4f_{7/2}$ was located at 74.66 and 71.36 eV, revealing a downshift of 0.24 eV and an upshift of 0.36 eV relative to that of *fct*-Pt−Co nanocrystals and pure Pt, respectively (Figure 4A). This variation in binding energy was primarily due to the existence of the compressively strained Pt shell with an *fcc* structure. In addition, it was observed that the signals from Co(II) were dramatically decreased, which might be due to the galvanic replacement reaction between the Pt(II) precursor and surface Co(II) oxides and the generation of dissoluble Co(III) species during the deposition of Pt (Figure 4B). Figure 4C shows the XPS spectrum of W $4f_{5/2}$ and W $4f_{7/2}$ peaks, revealing a great decrease of W(VI) or WO_3 and thus the removal of surface WO_3 during the overgrowth of Pt.

To achieve the optimal condition for the generation of Pt{111} facets on the surface, we need to induce the preferential overgrowth of Pt atoms on the {001} facets over

https://doi.org/10.1021/jacs.1c04160
J. Am. Chem. Soc. 2021, 143, 8509−8518

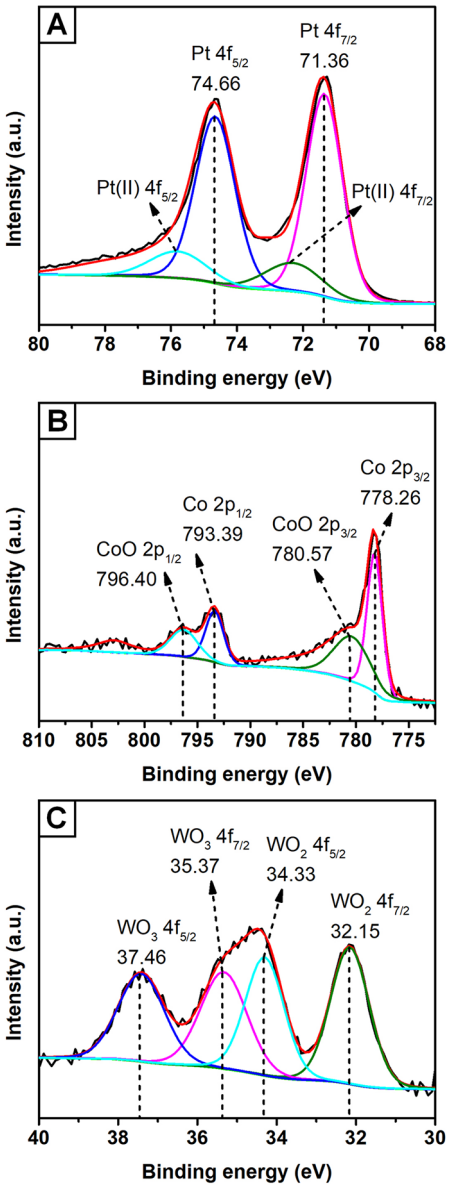

Figure 4. XPS spectra of the (A) Pt 4f, (B) Co 2p, and (C) W 4f recorded from the 8 nm *fct*-Pt−Co@Pt octahedral nanocrystals.

{111} facets of *fct*-Pt−Co truncated octahedral nanocrystals through a kinetic control. Figure S8 illustrates a plausible mechanism for the seed-mediated growth of Pt on nanocrystals. The deposition of Pt atoms was supposed to be initiated on the {001} facets of the *fct*-Pt−Co nanocrystals due to their higher surface energy relative to the {111} facets.[43−45] Upon deposition, the Pt adatoms could migrate to the edges and {111} facets through surface diffusion. The growth pattern of Pt was determined by the ratio between the rates responsible for atom deposition and surface diffusion (V_{dep}/V_{diff}).[44] The deposition rate can be directly tuned by varying the injection rate of the precursor. As shown in Figure S9A, if the Pt(II) precursor solution was injected rapidly, nanocrystals with irregular shapes and relatively large sizes were formed. This result suggests a higher deposition rate relative to surface diffusion, resulting in the overgrowth of Pt on both {111} and {001} facets. We also studied the impact of reaction temperature, which can alter both the surface diffusion and deposition rates of Pt atoms. When the reaction temperature was increased from 80 °C to 95 °C, cuboctahedral and truncated octahedral nanocrystals were obtained, indicating a greater surface diffusion rate over the deposition rate (Figure S9B). At a rapid injection rate and 95 °C, the final products contained irregular and concave octahedral nanocrystals, indicating the deposition rate was still greater than the surface diffusion rate (Figure S9C). When the two rates were balanced, the amount of the added Pt(II) precursor correlated well with the thickness of the Pt overlayers and thus the size of the particles. As shown in Figure S9D, increasing the amount of Pt(II) precursor to 9 mg resulted in concave octahedral nanocrystals with larger sizes and a broader size distribution.

In all these syntheses, citric acid was used as a weak reducing agent to help maintain the Pt atoms at a relatively low concentration and thus eliminate homogeneous nucleation. As such, the deposition rate could also be adjusted by varying the concentration of citric acid. When the amount of citric acid was decreased to 10 mg, for example, the majority of the products showed a truncated octahedral shape, indicating negligible deposition of Pt on the surface (Figure S10A). In contrast, when 60 mg of citric acid was added, the reduction of Pt(II) precursor was greatly facilitated due to the increase in reducing power, resulting in uneven deposition of Pt and the emergence of large octahedral nanocrystals (Figure S10B). Taken together, the conformal growth of Pt on carbon-supported *fct*-Pt−Co nanocrystals was highly dependent on the injection rate of the precursor, the reaction temperature, and the strength of the reducing agent. Only a proper combination of these parameters would result in the formation of *fct*-Pt−Co@Pt octahedral nanocrystals with a uniform size and smooth surface.

The different growth patterns and the corresponding products are summarized in Figure S11. Under $V_{dep}/V_{diff} \ll 1$, the growth was dominated by surface diffusion, enabling a conformal and uniform coating of Pt and thus the formation of *fct*-Pt−Co@Pt truncated octahedral nanocrystals via the layer-by-layer deposition of Pt adatoms. On the contrary, under $V_{dep}/V_{diff} \gg 1$, surface diffusion could be neglected and the deposition of Pt was not confined to the {001} facets, resulting in layer-plus-island growth and the formation of *fct*-Pt−Co@Pt nanocrystals with no control over the surface structure. When V_{dep} and V_{diff} were comparable, a portion of the Pt adatoms on the {001} facets migrated to the edges and {111} facets of the seeds, generating *fct*-Pt−Co@Pt octahedral or concave octahedral nanocrystals. For instance, when V_{dep}/V_{diff} was slightly less than 1, some of the Pt adatoms would stay on the {001} facets, whereas the rest would diffuse to the edges and {111} facets, leading to the formation of *fct*-Pt−Co@Pt octahedral nanocrystals. When V_{dep}/V_{diff} was slightly greater than 1, the deposition would be largely confined to the {001} facets, with only a small portion of the Pt adatoms migrating to the edges. Accordingly, the product became concave octahedral nanocrystals.

In addition to the changes in electronic and surface structure, the surface cleanliness of the nanocrystals during the synthesis was also analyzed by XPS and Fourier transform infrared spectroscopy (FTIR). As shown in Figure S12, the signals of N 1s (~398 eV) were detected from *fcc*-Pt−Co nanocrystals, indicating the presence of OAm on the surface and thus compromised cleanliness. The signals significantly dropped after annealing, which could be attributed to the desorption of OAm molecules from the surface at the elevated temperature.[46] Remarkably, no N 1s signal was detected for

https://doi.org/10.1021/jacs.1c04160
J. Am. Chem. Soc. 2021, 143, 8509−8518

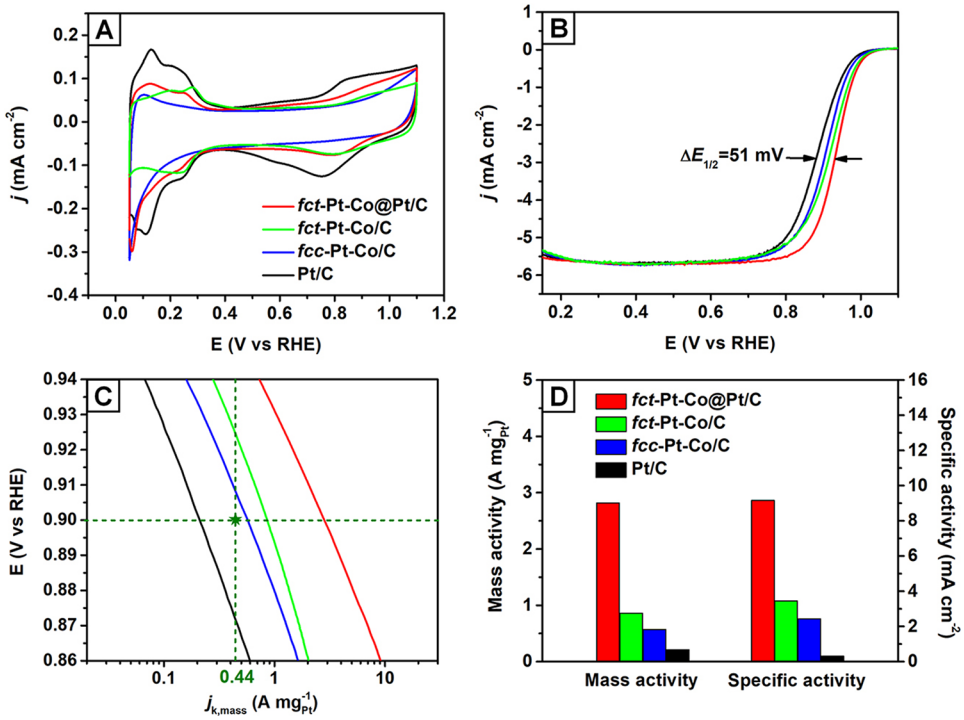

Figure 5. Electrocatalytic performance of the 8 nm *fct*-Pt−Co@Pt/C catalyst measured in the setting of a liquid half-cell. (A) CV curves of the *fct*-Pt−Co@Pt/C (red), *fct*-Pt−Co/C (green), *fcc*-Pt−Co/C (blue), and Pt/C (black) in a N_2-saturated $HClO_4$ solution. (B) Positive-going ORR polarization curves of the catalysts in an O_2-saturated $HClO_4$ solution. The currents were normalized to the geometric area of the rotating disk electrode (0.196 cm^2). (C) Mass activity Tafel plot for the catalysts. The green star indicates the 2025 mass activity target (0.44 A mg^{-1} at 0.90 V_{RHE}) set by DOE. (D) Mass activity and specific activity at 0.9 V_{RHE} based on the Pt mass loading and ECSAs calculated from the charges associated with H_{UPD}, respectively.

the *fct*-Pt−Co@Pt octahedral nanocrystals, suggesting that their surface was free of OAm. Figure S13 shows the FTIR spectra recorded from the three samples, revealing the C−H vibration peaks at 2920 and 2852 cm^{-1} and C−N vibration peak at 1072 cm^{-1} for both the *fcc*-Pt−Co and *fct*-Pt−Co samples. These peaks confirmed the presence of OAm on the surface of the nanocrystals.[47] In contrast, the peaks were absent after the deposition of Pt, further confirming the improvement in surface cleanliness.

Catalytic Performance of the 8 nm *fct*-Pt−Co@Pt Octahedral Nanocrystals. In a typical evaluation, the catalyst was loaded on a glassy carbon disk and then tested using the thin-film rotating disk electrode (TF-RDE) technique. Due to the absence of polymer stabilizer on the surface, all the procedures for postsynthesis treatments could be skipped. Cyclic voltammetry (CV) and linear scanning voltammetry were performed to evaluate the ORR performance of the catalyst by benchmarking against *fcc*-Pt−Co/C, *fct*-Pt−Co/C, and a state-of-the-art Pt/C catalyst (20 wt % of 3.2 nm Pt particles on Vulcan XC-72, Premetek Co.) at room temperature. According to the CV curves in Figure 5A and the average charges associated with the adsorption and desorption of hydrogen (H_{UPD}), the electrochemically active surface areas (ECSAs) of the catalysts were calculated to be 30.8, 24.9, 23.4, and 67.7 $m^2\ g_{Pt}^{-1}$ for *fct*-Pt−Co@Pt/C, *fct*-Pt−Co/C, *fcc*-Pt−Co/C, and Pt/C, respectively. The large difference in CV curves between *fcc*-Pt−Co/C and *fct*-Pt−Co/C could be attributed to thermal activation and enrichment of Pt on the surface during the reductive annealing.[46,48,49] The CV curve of the *fct*-Pt−Co@Pt octahedral nanocrystals exhibited features typical of Pt, and the voltametric peaks matched those of Pd@Pt octahedral nanocrystals with a polymer-free surface, indicating clean Pt{111} facets on the surface of the nanocrystals.[50] Figure 5B shows the positive-going ORR polarization curves of the catalysts. The *fct*-Pt−Co@Pt/C exhibited a half-wave potential ($E_{1/2}$) of 0.931 V_{RHE}, which was 51 mV more positive than that of the Pt/C even though the Pt loading of the former was much lower (1 vs 2 μg). The kinetic current was then calculated based on the Koutecky−Levich equation and normalized against the ECSA and the mass loading of Pt to obtain the specific and mass activities at 0.9 V_{RHE}, respectively.

As summarized in Table 1, the specific activity of the *fct*-Pt−Co@Pt/C was calculated to be 9.16 mA cm^{-2}, 3.8 and 2.7 times respectively greater than those of both the *fcc*-Pt−Co/C (2.44 mA cm^{-2}) and *fct*-Pt−Co/C (3.45 mA cm^{-2}). The large enhancement in specific activity could be attributed to three major factors: (i) the ordered incorporation of Co into the specific lattice points of Pt and thus stronger ligand and strain effects; (ii) the exposure of well-defined Pt{111} facets with the anisotropic strains; and (iii) the absence of surfactant and thus fully exposed active sites on the surface. Benefiting from the great enhancement in specific activity, together with a high ECSA, the *fct*-Pt−Co@Pt/C showed a mass activity of 2.82 A mg^{-1} (Figure 5, C and D), 13.4 and 6.4 times respectively greater than that of the Pt/C catalyst (0.21 A mg^{-1}) and the 2025 target set by the U.S. Department of Energy (DOE, 0.44 A mg^{-1} at 0.9 V_{RHE} for membrane electrode assembly). At a comparable Pt loading, the mass activity of the *fct*-Pt−Co@Pt/C catalyst is among the highest reported for the representative Pt−Co nanocrystals with an *fcc* or *fct* structure (Table S3).[26,28,29,41,51−56]

https://doi.org/10.1021/jacs.1c04160
J. Am. Chem. Soc. 2021, 143, 8509−8518

Table 1. Electrochemically Active Surface Areas (ECSAs), Specific Activities (SA), and Mass Activities (MA) of the *fct*-Pt−Co@Pt/C, *fct*-Pt−Co/C, *fcc*-Pt−Co/C, and Commercial Pt/C Catalysts before and after Different Cycles of ADT

sample	cycles of ADT	ECSA (m^2 g_{Pt}^{-1})	SA at 0.9 V (mA cm^{-2})	MA at 0.9 V (A mg_{Pt}^{-1})
fct-Pt−Co@Pt/C	initial	30.8	9.16	2.82
	10 000	29.7	9.02	2.68
	20 000	31.6	7.66	2.42
	30 000	30.9	7.21	2.23
fct-Pt−Co/C	initial	24.9	3.45	0.86
	10 000	22.5	2.80	0.63
	20 000	21.9	2.56	0.56
fcc-Pt−Co/C	initial	23.4	2.44	0.57
	10 000	20.8	1.54	0.32
	20 000	22.1	1.04	0.23
Pt/C	initial	67.7	0.31	0.21
	10 000	42.9	0.21	0.09

The durability of the catalyst was evaluated through accelerated durability test (ADT) by applying continuous potential cycling (up to 30 000 cycles) in an O_2-saturated $HClO_4$ solution at room temperature. After different cycles of ADT, the ECSAs of the catalysts were derived from the corresponding CV curves (Figures 6A, S14A, S15A, and S16A). The data recorded every 10 000 cycles show that the $E_{1/2}$ of Pt/C, *fcc*-Pt−Co/C, and *fct*-Pt−Co/C negatively shifted by 39, 27, and 18 mV relative to those of the pristine catalysts, respectively (Figures S14B, S15B, and S16B). In contrast, we observed a downshift of only 11 mV for the *fct*-Pt−Co@Pt/C even after 30 000 cycles of ADT, demonstrating the remarkable durability of the catalyst under the standard liquid half-cell testing condition (Figure 6B). As shown in Figure 6C, the ECSA of the *fct*-Pt−Co@Pt/C was maintained at a stable level with almost no loss after the ADT. Figure 6D shows the changes in mass activity for different catalysts before and after ADT. The mass activities of the Pt/C, *fcc*-Pt−Co/C, and *fct*-Pt−Co/C catalysts dropped by 57%, 60%, and 35% after 10 000, 20 000, and 20 000 cycles of potential sweeping, respectively. The loss in mass activity of both *fcc*-Pt−Co/C and *fct*-Pt−Co/C catalysts during the ADT correlated well with the degradation in specific activity (Figure S17), suggesting the leaching of Co and the loss of active sites on the surface. Comparatively, the mass and specific activities dropped by only 21% after 30 000 cycles of ADT, confirming the great potential of the *fct*-Pt−Co@Pt/C as a viable ORR catalyst.

To achieve a better understanding of their difference in durability, we examined the catalysts after the ADT tests by TEM. For the Pt/C, severe agglomeration and detachment of the Pt nanoparticles were observed after 10 000 cycles of ADT (Figure S18A). Notably, the *fcc*-Pt−Co/C underwent obvious changes in both shape and composition (Figure S18B). Compared to the initial sample, the percentage of {111} facets on the surface decreased, together with a large increase of Pt/Co atomic ratio from 0.69 to 8.09 and a Co loss of 91% due to the electrochemical leaching of Co during the ADT, leading to diminished specific and mass activities (Figure S19 and Table S1). For the *fct*-Pt−Co/C, slight agglomeration and a Co loss of 64% occurred after the ADT, indicating the enhanced electrochemical stability of the nanocrystals after annealing (Figures S18C and S20 and Table S1). In comparison, the *fct*-Pt−Co@Pt/C essentially retained their original shape, and no obvious aggregation was observed even after 30 000 cycles of ADT (Figure 7A). The well-preserved dispersion of nanocrystals could be attributed to the enhanced metal−support interaction that was achieved by the removal of ligand from the metal−support interface.[57,58] As shown in Figure 7, B and C, the alternating high (Pt) and low (Co) *Z*-contrast stripes with a lattice fringe spacing of 3.7 Å along the

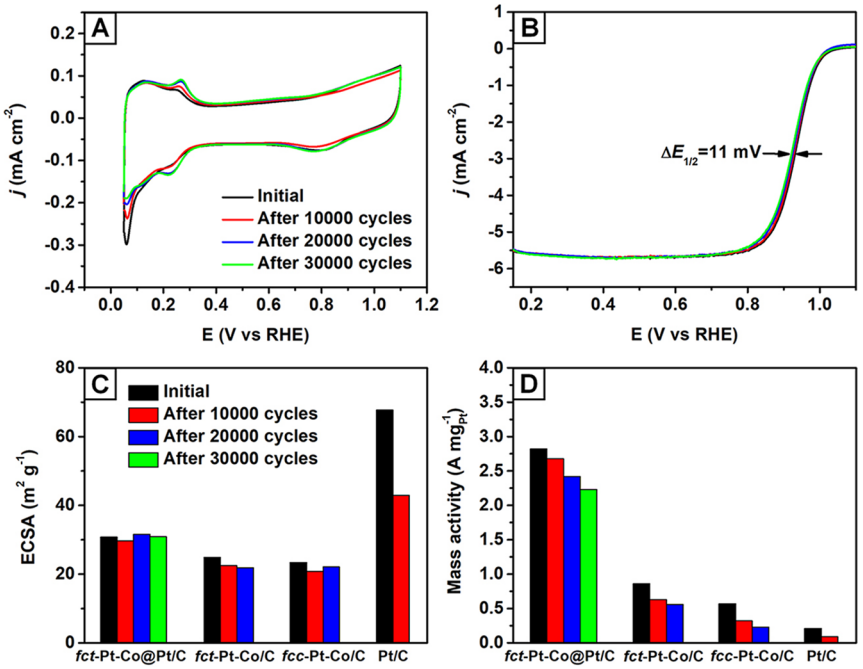

Figure 6. (A) CV and (B) ORR polarization curves recorded from the *fct*-Pt−Co@Pt/C catalyst before and after different cycles of ADT, respectively. (C) ECSA and (D) mass activity of the catalysts at 0.9 V_{RHE} before and after different cycles of ADT. Each ADT test was performed using the same *fct*-Pt−Co@Pt/C, *fct*-Pt−Co/C, *fcc*-Pt−Co/C, or Premetek Pt/C electrode.

https://doi.org/10.1021/jacs.1c04160
J. Am. Chem. Soc. 2021, 143, 8509−8518

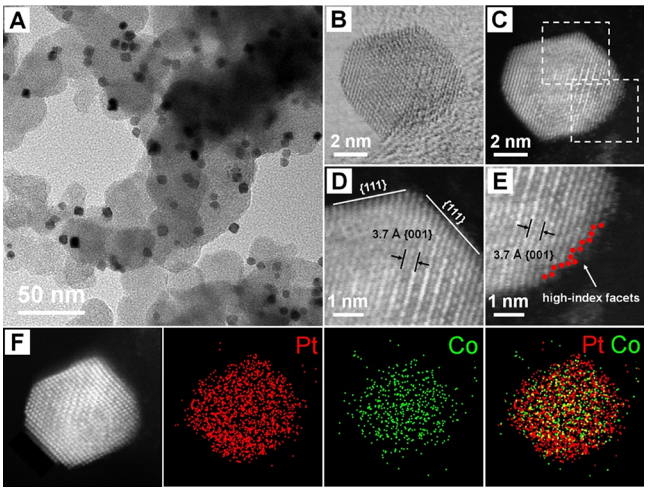

Figure 7. (A) TEM image of the *fct*-Pt−Co@Pt/C after 30 000 cycles of ADT. (B) HAABF- and (C) HAADF-STEM images of an individual *fct*-Pt−Co@Pt nanocrystal. (D, E) Atomic-resolution STEM images taken from the regions marked by boxes in panel (C). (F) HAADF-STEM image and EDX mapping (Pt/red, Co/green) of an individual *fct*-Pt−Co@Pt nanocrystal, confirming the preservation of Co after 30 000 cycles of ADT.

[001] direction still existed in the nanocrystal, demonstrating the well-preserved *fct* structure. Figure 7, D and E, shows that the nanocrystal was still terminated by {111} facets on the side faces, together with the emergence of high-index facets at the corners. Moreover, EDX elemental mapping of a representative nanocrystal also confirmed that a substantial amount of Co was retained after potential cycles (Figure 7F). The reduced loss of Co in the nanocrystals was also confirmed by ICP-MS, XPS, and EDX, revealing an increase of Pt/Co atomic ratio from 1.17 to 1.56 and a Co loss of 25% (Figures S21 and S22; Tables S1 and S4). The remarkable durability can be attributed to the robust chemical, structural, and shape stability of the nanocrystals as a result of the highly ordered metal atom arrangement and d−d orbital interactions, stabilizing the Co atoms against leaching.[28] Additionally, the relatively large lattice mismatch (2.8% along the [100] and [010] directions and 4.6% along the [001] direction) between the *fcc*-Pt shell and *fct*-Pt−Co core also helped reduce the diffusion of Co from the core into the Pt overlayers (Table S2). Besides, the lattice contraction might have a stabilization effect on the low-coordinate atoms located at vertex and edge sites and weakened the E_0 at these sites to an optimal value. Moreover, the anisotropic surface strain also helped lower the surface energy of the nanocrystals, stabilizing the active Pt surface against dissolution during the catalysis.[29]

CONCLUSION

We have demonstrated the synthesis of an ORR catalyst based on 8 nm *fct*-Pt−Co@Pt octahedral nanocrystals featuring a Pt−Co intermetallic core, a Pt shell of three or four atom layers, well-defined {111} facets, and a clean surface free of surfactants. The as-obtained nanocrystals exhibited superior mass and specific activities toward ORR, which were more than 13 and 29 times respectively greater than those of the commercial Pt/C catalyst. The intermetallic catalyst also showed robust chemical, structural, and shape stability and thus remarkable durability, with activity largely retained even after 30 000 cycles of ADT. The great ORR performance of the catalyst originated from the ordered incorporation of Co atoms into the Pt lattice and the exposure of Pt{111} facets with an anisotropic strain and maximal active sites on the surface, optimizing the E_0 and stabilizing the Co atoms under corrosive ORR condition. Taken together, this work not only highlights the ability and importance of surface faceting of intermetallic nanocrystals at the atomic scale but also offers an efficient strategy for the rational development of Pt-based catalysts with controlled atomic distributions, crystal phase, and surface geometry for applications in fuel cells and related devices.

ASSOCIATED CONTENT

Supporting Information

The Supporting Information is available free of charge at https://pubs.acs.org/doi/10.1021/jacs.1c04160.

TEM and HAADF-STEM images, XPS, FTIR, EDX, ICP-MS, and electrochemical performance of the catalysts, Figures S1−S22, Tables S1−S4 (PDF)

AUTHOR INFORMATION

Corresponding Author

Younan Xia − *The Wallace H. Coulter Department of Biomedical Engineering, Georgia Institute of Technology and Emory University, Atlanta, Georgia 30332, United States; School of Chemistry and Biochemistry, Georgia Institute of Technology, Atlanta, Georgia 30332, United States;* orcid.org/0000-0003-2431-7048; Email: younan.xia@bme.gatech.edu

Authors

Minghao Xie − *School of Chemistry and Biochemistry, Georgia Institute of Technology, Atlanta, Georgia 30332, United States;* orcid.org/0000-0003-3781-5118

Zhiheng Lyu − *School of Chemistry and Biochemistry, Georgia Institute of Technology, Atlanta, Georgia 30332, United States*

Ruhui Chen − *School of Chemistry and Biochemistry, Georgia Institute of Technology, Atlanta, Georgia 30332, United States*

Min Shen − *The Wallace H. Coulter Department of Biomedical Engineering, Georgia Institute of Technology and Emory University, Atlanta, Georgia 30332, United States*

Zhenming Cao − *The Wallace H. Coulter Department of Biomedical Engineering, Georgia Institute of Technology and Emory University, Atlanta, Georgia 30332, United States*

Complete contact information is available at: https://pubs.acs.org/10.1021/jacs.1c04160

Notes

The authors declare no competing financial interest.

ACKNOWLEDGMENTS

This work was supported in part by a grant from the NSF (CHE-1804970) and start-up funds from the Georgia Institute of Technology. TEM imaging, high-resolution STEM imaging, EDX, XRD, and XPS analyses were performed at the Georgia Tech Institute for Electronics and Nanotechnology, a member of the National Nanotechnology Coordinated Infrastructure, which is supported by the NSF (ECCS-2025462).

REFERENCES

(1) Song, C.; Zhang, J. Electrocatalytic Oxygen Reduction Reaction. In *PEM Fuel Cell Electrocatalysts and Catalyst Layers: Fundamentals and Applications*; Springer London: London, 2008; pp 89−134.

(2) Vielstich, W.; Lamm, A.; Gasteiger, H. A. *Handbook of Fuel Cells−Fundamentals, Technology and Applications*; John Wiley & Sons: Chichester, U.K., 2003.

(3) Shao, M. *Electrocatalysis in Fuel Cells: A Non- and Low-Platinum Approach*; Springer: London, 2013.

(4) Steele, B. C. H.; Heinzel, A. Materials for Fuel-Cell Technologies. *Nature* **2001**, *414*, 345−352.

(5) Debe, M. K. Electrocatalyst Approaches and Challenges for Automotive Fuel Cells. *Nature* **2012**, *486*, 43−51.

(6) Guo, S.; Li, D.; Zhu, H.; Zhang, S.; Markovic, N. M.; Stamenkovic, V. R.; Sun, S. FePt and CoPt Nanowires as Efficient Catalysts for the Oxygen Reduction Reaction. *Angew. Chem., Int. Ed.* **2013**, *52*, 3465−3468.

(7) Stamenkovic, V. R.; Fowler, B.; Mun, B. S.; Wang, G.; Ross, P. N.; Lucas, C. A.; Markovic, N. M. Improved Oxygen Reduction Activity on $Pt_3Ni(111)$ Via Increased Surface Site Availability. *Science* **2007**, *315*, 493−497.

(8) Cui, C.; Gan, L.; Heggen, M.; Rudi, S.; Strasser, P. Compositional Segregation in Shaped Pt Alloy Nanoparticles and Their Structural Behaviour During Electrocatalysis. *Nat. Mater.* **2013**, *12*, 765−771.

(9) Zhang, J.; Yang, H.; Fang, J.; Zou, S. Synthesis and Oxygen Reduction Activity of Shape-Controlled Pt_3Ni Nanopolyhedra. *Nano Lett.* **2010**, *10*, 638−644.

(10) Choi, S. I.; Xie, S.; Shao, M.; Odell, J. H.; Lu, N.; Peng, H.; Protsailo, L.; Guerrero, S.; Park, J. H.; Xia, X.; Wang, J.; Kim, M. J.; Xia, Y. Synthesis and Characterization of 9 nm Pt-Ni Octahedra with a Record High Activity of 3.3 A/mg_{Pt} for the Oxygen Reduction Reaction. *Nano Lett.* **2013**, *13*, 3420−3425.

(11) Huang, X.; Zhao, Z.; Cao, L.; Chen, Y.; Zhu, E.; Lin, Z.; Li, M.; Yan, A.; Zettl, A.; Wang, Y.; Duan, X.; Mueller, T.; Huang, Y. High-Performance Transition Metal-Doped Pt_3Ni Octahedra for Oxygen Reduction Reaction. *Science* **2015**, *348*, 1230−1234.

(12) Chen, C.; Kang, Y.; Huo, Z.; Zhu, Z.; Huang, W.; Xin, H. L.; Snyder, J. D.; Li, D.; Herron, J. A.; Mavrikakis, M.; Chi, M.; More, K. L.; Li, Y.; Markovic, N. M.; Somorjai, G. A.; Yang, P.; Stamenkovic, V. R. Highly Crystalline Multimetallic Nanoframes with Three-Dimensional Electrocatalytic Surfaces. *Science* **2014**, *343*, 1339−1343.

(13) Lim, B.; Jiang, M.; Camargo, P. H. C.; Cho, E. C.; Tao, J.; Lu, X.; Zhu, Y.; Xia, Y. Pd-Pt Bimetallic Nanodendrites with High Activity for Oxygen Reduction. *Science* **2009**, *324*, 1302−1305.

(14) Oezaslan, M.; Hasché, F.; Strasser, P. Pt-Based Core-Shell Catalyst Architectures for Oxygen Fuel Cell Electrodes. *J. Phys. Chem. Lett.* **2013**, *4*, 3273−3291.

(15) Wang, J.; Inada, H.; Wu, L.; Zhu, Y.; Choi, Y.; Liu, P.; Zhou, W.-P.; Adzic, R. R. Oxygen Reduction on Well-Defined Core-Shell Nanocatalysts: Particle Size, Facet, and Pt Shell Thickness Effects. *J. Am. Chem. Soc.* **2009**, *131*, 17298−17302.

(16) Xie, S.; Choi, S.-I.; Lu, N.; Roling, L. T.; Herron, J. A.; Zhang, L.; Park, J.; Wang, J.; Kim, M. J.; Xie, Z.; Mavrikakis, M.; Xia, Y. Atomic Layer-by-Layer Deposition of Pt on Pd Nanocubes for Catalysts with Enhanced Activity and Durability toward Oxygen Reduction. *Nano Lett.* **2014**, *14*, 3570−3576.

(17) Peng, Z.; Yang, H. Synthesis and Oxygen-Reduction Electrocatalytic Property of Pt-on-Pd Bimetallic Heteronanostructures. *J. Am. Chem. Soc.* **2009**, *131*, 7542−7543.

(18) Choi, S. I.; Shao, M.; Lu, N.; Ruditskiy, A.; Peng, H.; Park, J.; Guerrero, S.; Wang, J.; Kim, M. J.; Xia, Y. Synthesis and Characterization of Pd@Pt-Ni Core-Shell Octahedra with High Activity toward Oxygen Reduction. *ACS Nano* **2014**, *8*, 10363−10371.

(19) Park, J.; Zhang, L.; Choi, S. I.; Roling, L. T.; Lu, N.; Herron, J. A.; Xie, S.; Wang, J.; Kim, M. J.; Mavrikakis, M.; Xia, Y. Atomic Layer-by-Layer Deposition of Platinum on Palladium Octahedra for Enhanced Catalysts toward the Oxygen Reduction Reaction. *ACS Nano* **2015**, *9*, 2635−2647.

(20) Cui, C.; Gan, L.; Li, H.-H.; Yu, S.-H.; Heggen, M.; Strasser, P. Octahedral PtNi Nanoparticle Catalysts: Exceptional Oxygen Reduction Activity by Tuning the Alloy Particle Surface Composition. *Nano Lett.* **2012**, *12*, 5885−5889.

(21) Wu, J.; Gross, A.; Yang, H. Shape and Composition-Controlled Platinum Alloy Nanocrystals Using Carbon Monoxide as Reducing Agent. *Nano Lett.* **2011**, *11*, 798−802.

(22) Choi, S.-I.; Xie, S.; Shao, M.; Lu, N.; Guerrero, S.; Odell, J. H.; Park, J.; Wang, J.; Kim, M. J.; Xia, Y. Controlling the Size and Composition of Nanosized Pt-Ni Octahedra To Optimize Their Catalytic Activities toward the Oxygen Reduction Reaction. *ChemSusChem* **2014**, *7*, 1476−1483.

(23) Stamenkovic, V. R.; Mun, B. S.; Mayrhofer, K. J. J.; Ross, P. N.; Markovic, N. M.; Rossmeisl, J.; Greeley, J.; Nørskov, J. K. Changing the Activity of Electrocatalysts for Oxygen Reduction by Tuning the Surface Electronic Structure. *Angew. Chem., Int. Ed.* **2006**, *45*, 2897−2901.

(24) Stamenkovic, V. R.; Mun, B. S.; Arenz, M.; Mayrhofer, K. J. J.; Lucas, C. A.; Wang, G.; Ross, P. N.; Markovic, N. M. Trends in Electrocatalysis on Extended and Nanoscale Pt-Bimetallic Alloy Surfaces. *Nat. Mater.* **2007**, *6*, 241−247.

(25) Greeley, J.; Stephens, I. E. L.; Bondarenko, A. S.; Johansson, T. P.; Hansen, H. A.; Jaramillo, T. F.; Rossmeisl, J.; Chorkendorff, I.; Nørskov, J. K. Alloys of Platinumand Early TransitionMetals as Oxygen Reduction Electrocatalysts. *Nat. Chem.* **2009**, *1*, 552−556.

(26) Wang, D.; Xin, H. L.; Hovden, R.; Wang, H.; Yu, Y.; Muller, D. A.; DiSalvo, F. J.; Abruna, H. D. Structurally Ordered Intermetallic Platinum-Cobalt Core-Shell Nanoparticles with Enhanced Activity and Stability as Oxygen Reduction Electrocatalysts. *Nat. Mater.* **2013**, *12*, 81−87.

(27) Chong, L.; Wen, J. G.; Kubal, J.; Sen, F.; Zou, J.; Greeley, J.; Chan, M.; Barkholtz, H.; Ding, W.; Liu, D. Ultralow-Loading Platinum-Cobalt Fuel Cell Catalysts Derived from Imidazolate Frameworks. *Science* **2018**, *362*, 1276−1281.

(28) Li, J.; Sharma, S.; Liu, X.; Pan, Y.; Spendelow, J. S.; Chi, M.; Jia, Y.; Zhang, P.; Cullen, D. A.; Xi, Z.; Lin, H.; Yin, Z.; Shen, B.; Muzzio, M.; Yu, C.; Kim, Y. S.; Peterson, A. A.; More, K. L.; Zhu, H.; Sun, S. Hard-Magnet $L1_0$-CoPt Nanoparticles Advance Fuel Cell Catalysis. *Joule* **2019**, *3*, 124−135.

(29) Liang, J.; Li, N.; Zhao, Z.; Ma, L.; Wang, X.; Li, S.; Liu, X.; Wang, T.; Du, Y.; Lu, G.; Han, J.; Huang, Y.; Su, D.; Li, Q. Tungsten-Doped $L1_0$-PtCo Ultrasmall Nanoparticles as a High-Performance Fuel Cell Cathode. *Angew. Chem., Int. Ed.* **2019**, *58*, 15471−15477.

(30) Wang, T.; Liang, J.; Zhao, Z.; Li, S.; Lu, G.; Xia, Z.; Wang, C.; Luo, J.; Han, J.; Ma, C.; Huang, Y.; Li, Q. Sub-6 nm Fully Ordered $L1_0$-Pt-Ni-Co Nanoparticles Enhance Oxygen Reduction via Co Doping Induced Ferromagnetism Enhancement and Optimized Surface Strain. *Adv. Energy Mater.* **2019**, *9*, 1803771.

(31) Li, J.; Xi, Z.; Pan, Y.; Spendelow, J. S.; Duchesne, P. N.; Su, D.; Li, Q.; Yu, C.; Yin, Z.; Shen, B.; Kim, Y. S.; Zhang, P.; Sun, S. Fe Stabilization by Intermetallic $L1_0$-FePt and Pt Catalysis Enhancement in $L1_0$-FePt/Pt Nanoparticles for Efficient Oxygen Reduction Reaction in Fuel Cells. *J. Am. Chem. Soc.* **2018**, *140*, 2926−2932.

(32) Brodsky, C. N.; Young, A. P.; Ng, K. C.; Kuo, C. H.; Tsung, C. K. Electrochemically Induced Surface Metal Migration in Well-Defined Core-Shell Nanoparticles and Its General Influence on Electrocatalytic Reactions. *ACS Nano* **2014**, *8*, 9368−9378.

(33) Li, J.; Sharma, S.; Wei, K.; Chen, Z.; Morris, D.; Lin, H.; Zeng, C.; Chi, M.; Yin, Z.; Muzzio, M.; Shen, M.; Zhang, P.; Peterson, A. A.; Sun, S. Anisotropic Strain Tuning of $L1_0$ Ternary Nanoparticles for Oxygen Reduction. *J. Am. Chem. Soc.* **2020**, *142*, 19209−19216.

(34) Wang, Z.; Yao, X.; Kang, Y.; Miao, L.; Xia, D.; Gan, L. Structurally Ordered Low-Pt Intermetallic Electrocatalysts toward Durably High Oxygen Reduction Reaction Activity. *Adv. Funct. Mater.* **2019**, *29*, 1902987.

(35) Chen, H.; Wang, D.; Yu, Y.; Newton, K. A.; Muller, D. A.; Abruña, H.; DiSalvo, F. J. A Surfactant-Free Strategy for Synthesizing

https://doi.org/10.1021/jacs.1c04160
J. Am. Chem. Soc. 2021, 143, 8509−8518

and Processing Intermetallic Platinum-Based Nanoparticle Catalysts. *J. Am. Chem. Soc.* **2012**, *134*, 18453−18459.
(36) Li, J.; Sun, S. Intermetallic Nanoparticles: Synthetic Control and Their Enhanced Electrocatalysis. *Acc. Chem. Res.* **2019**, *52*, 2015−2025.
(37) Yan, Y.; Du, J. S.; Gilroy, K. D.; Yang, D. R.; Xia, Y.; Zhang, H. Intermetallic Nanocrystals: Syntheses and Catalytic Applications. *Adv. Mater.* **2017**, *29*, 1605997.
(38) Xiao, W.; Lei, W.; Gong, M.; Xin, H.; Wang, D. Recent Advances of Structurally Ordered Intermetallic Nanoparticles for Electrocatalysis. *ACS Catal.* **2018**, *8*, 3237−3256.
(39) Chen, X.; Wu, G.; Chen, J.; Chen, X.; Xie, Z.; Wang, X. Synthesis of "Clean" and Well-Dispersive Pd Nanoparticles with Excellent Electrocatalytic Property on Graphene Oxide. *J. Am. Chem. Soc.* **2011**, *133*, 3693−3695.
(40) Zhang, C.; Hwang, S. Y.; Trout, A.; Peng, Z. Solid-State Chemistry-Enabled Scalable Production of Octahedral Pt-Ni Alloy Electrocatalyst for Oxygen Reduction Reaction. *J. Am. Chem. Soc.* **2014**, *136*, 7805−7808.
(41) He, C.; Zhang, S.; Tao, J.; Shen, P. One-Step Solid State Synthesis of PtCo Nanocubes/Graphene Nanocomposites as Advanced Oxygen Reduction Reaction Electrocatalysts. *J. Catal.* **2018**, *362*, 85−93.
(42) Choi, R.; Choi, S.-I.; Choi, C. H.; Nam, K. M.; Woo, S. I.; Park, J. T.; Han, S. Designed Synthesis of Well-Defined Pd@Pt Core-Shell Nanoparticles with Controlled Shell Thickness as Efficient Oxygen Reduction Electrocatalysts. *Chem. - Eur. J.* **2013**, *19*, 8190−8198.
(43) Chi, M.; Wang, C.; Lei, Y.; Wang, G.; Li, D.; More, K. L.; Lupini, A.; Allard, L. F.; Markovic, N. M.; Stamenkovic, V. R. Surface Faceting and Elemental Diffusion Behaviour at Atomic Scale for Alloy Nanoparticles During in Situ Annealing. *Nat. Commun.* **2015**, *6*, 8925.
(44) Ye, H.; Wang, Q.; Catalano, M.; Lu, N.; Vermeylen, J.; Kim, M. J.; Liu, Y.; Sun, Y.; Xia, X. Ru Nanoframes with an fcc Structure and Enhanced Catalytic Properties. *Nano Lett.* **2016**, *16*, 2812−2817.
(45) Xia, Y.; Xia, X.; Peng, H. C. Shape-Controlled Synthesis of Colloidal Metal Nanocrystals: Thermodynamic versus Kinetic Products. *J. Am. Chem. Soc.* **2015**, *137*, 7947−7966.
(46) Li, D. G.; Wang, C.; Tripkovic, D.; Sun, S.; Markovic, N. M.; Stamenkovic, V. R. Surfactant Removal for Colloidal Nanoparticles from Solution Synthesis: The Effect on Catalytic Performance. *ACS Catal.* **2012**, *2*, 1358−1362.
(47) Mourdikoudis, S.; Liz-Marzan, L. M. Oleylamine in Nanoparticle Synthesis. *Chem. Mater.* **2013**, *25*, 1465−1476.
(48) Wang, Z.; Yao, X.; Kang, Y.; Miao, L.; Xia, D.; Gan, L. Structurally Ordered Low-Pt Intermetallic Electrocatalysts toward Durably High Oxygen Reduction Reaction Activity. *Adv. Funct. Mater.* **2019**, *29*, 1902987.
(49) Guntern, Y. T.; Okatenko, V.; Pankhurst, J.; Varandili, S. B.; Iyengar, P.; Koolen, C.; Stoian, D.; Vavra, J.; Buonsanti, R. Colloidal Nanocrystals as Electrocatalysts with Tunable Activity and Selectivity. *ACS Catal.* **2021**, *11*, 1248−1295.
(50) Bao, S.; Vara, M.; Yang, X.; Zhou, S.; Figueroa-Cosme, L.; Park, J.; Luo, M.; Xie, Z.; Xia, Y. Facile Synthesis of Pd@Pt_{3-4L} Core-Shell Octahedra with a Clean Surface and Thus Enhanced Activity toward Oxygen Reduction. *ChemCatChem* **2017**, *9*, 414−419.
(51) Luo, M.; Sun, Y.; Qin, Y.; Chen, S.; Li, Y.; Li, C.; Yang, Y.; Wu, D.; Xu, N.; Xing, Y.; Wang, L.; Gao, P.; Guo, S. Surface and Near-Surface Engineering of PtCo Nanowires at Atomic Scale for Enhanced Electrochemical Sensing and Catalysis. *Chem. Mater.* **2018**, *30*, 6660−6667.
(52) Choi, D. S.; Robertson, A. W.; Warner, J. H.; Kim, S. O.; Kim, H. Low-Temperature Chemical Vapor Deposition Synthesis of Pt-Co Alloyed Nanoparticles with Enhanced Oxygen Reduction Reaction Catalysis. *Adv. Mater.* **2016**, *28*, 7115−7122.
(53) Choi, J.; Cho, J.; Roh, C. W.; Kim, B. S.; Choi, M. S.; Jeong, H.; Ham, H. C.; Lee, H. Au-Doped PtCo/C Catalyst Preventing Co Leaching for Proton Exchange Membrane Fuel Cells. *Appl. Catal., B* **2019**, *247*, 142−149.
(54) Kuttiyiel, K. A.; Kattel, S.; Cheng, S.; Lee, J. H.; Wu, L.; Zhu, Y.; Park, G. G.; Liu, P.; Sasaki, K.; Chen, J. G.; Adzic, R. R. Au-Doped Stable $L1_0$ Structured Platinum Cobalt Ordered Intermetallic Nanoparticle Catalysts for Enhanced Electrocatalysis. *ACS Appl. Energy Mater.* **2018**, *1*, 3771−3777.
(55) Chen, Q.; Cao, Z.; Du, G.; Kuang, Q.; Huang, J.; Xie, Z.; Zheng, L. Excavated Octahedral Pt-Co Alloy Nanocrystals Built with Ultrathin Nanosheets as Superior Multifunctional Electrocatalysts for Energy Conversion Applications. *Nano Energy* **2017**, *39*, 582−589.
(56) Lee, S.; Jang, J. H.; Jang, I.; Choi, D.; Lee, K. S.; Ahn, D.; Kang, Y. S.; Park, H. Y.; Yoo, S. J. Development of Robust Pt Shell through Organic Hydride Donor in PtCo@Pt Core-Shell Electrocatalysts for Highly Stable Proton Exchange Membrane Fuel Cells. *J. Catal.* **2019**, *379*, 112−120.
(57) Dai, Y.; Lu, P.; Cao, Z.; Campbell, C. T.; Xia, Y. The Physical Chemistry and Materials Science Behind Sinter-Resistant Catalysts. *Chem. Soc. Rev.* **2018**, *47*, 4314−4331.
(58) Cheng, H.; Cao, Z.; Chen, Z.; Zhao, M.; Xie, M.; Lyu, Z.; Zhu, Z.; Chi, M.; Xia, Y. Catalytic System Based on Sub-2 nm Pt Particles and Its Extraordinary Activity and Durability for Oxygen Reduction. *Nano Lett.* **2019**, *19*, 4997−5002.

https://doi.org/10.1021/jacs.1c04160
J. Am. Chem. Soc. 2021, 143, 8509−8518